Small

NANO · MICRO small
www.small-journal.com

RESEARCH ARTICLE

Coupled Role of Zn^{2+} Reversibility and Reduced Water Activity in Achieving Stable Mild-Aqueous Zn||MnO_2 Batteries

Varun R. Kankanallu[1] | Adesanmi Adeniyi[1] | Jianming Bai[2] | Hui Zhong[2] | Ruipeng Li[2] | Honghu Zhang[2] | Xiao Tong[3] | Esther S. Takeuchi[1,4,5,6] | Amy C. Marschilok[1,4,5,6] | Kenneth J. Takeuchi[1,4,5,6] | Mingyuan Ge[2] | Yu-chen Karen Chen-Wiegart[1,2]

[1]Department of Materials Science and Chemical Engineering, Stony Brook University, Stony Brook, New York, USA | [2]National Synchrotron Light Source II, Brookhaven National Laboratory, Upton, New York, USA | [3]Center for Functional Nanomaterials, Brookhaven National Laboratory, Upton, New York, USA | [4]Energy and Photon Sciences Directorate, Brookhaven National Laboratory, Upton, New York, USA | [5]Department of Chemistry, Stony Brook University, Stony Brook, New York, USA | [6]Institute of Sustainability, Electrification, and Energy, Energy (I:SEE), Stony Brook University, Stony Brook, New York, USA

Correspondence: Varun R. Kankanallu (kankanallu.varun@stonybrook.edu) | Yu-chen Karen Chen-Wiegart (Karen.Chen-Wiegart@stonybrook.edu)

Received: 18 December 2025 | **Revised:** 8 June 2026 | **Accepted:** 3 July 2026

Keywords: aqueous solution | cathode | electrolyte | energy storage | kinetics | redox | solvation | water activity

ABSTRACT

Aqueous Zn||MnO_2 batteries are promising for large-scale energy storage but suffer from capacity fading due to irreversible transformations at the MnO_2 cathode. Achieving structural reversibility under long-term cycling remains a central challenge. Here, we show that tuning the electrolyte solvation environment can directly stabilize Mn redox chemistry and lattice evolution in mild-aqueous Zn||ε-MnO_2 batteries. Using dimethyl sulfoxide (DMSO) as a co-solvent to lower water activity and reorganize the solvation structure, we reveal through operando X-ray diffraction that the modified electrolyte promotes reversible Zn^{2+} intercalation despite slower transport kinetics. Complementary X-ray photoelectron spectroscopy shows that conventional aqueous electrolytes induce strong Mn-valence gradients between surface and bulk, whereas DMSO suppresses these gradients and maintains uniform redox states. Collectively, these results demonstrate that electrolyte solvation engineering can mitigate parasitic reactions and enable structurally reversible MnO_2 redox processes, establishing a holistic pathway to enhance the long-term stability of mild-aqueous Zn-based batteries.

1 | Introduction

Aqueous Zn-ion batteries (AZIBs) have emerged as sustainable, intrinsically safe, and low-cost energy storage systems. The Zn metal anode offers a low redox potential (−0.76 V vs. SHE), high theoretical capacity (820 mAh g^{-1}), and compatibility with aqueous electrolytes, making it highly attractive for large-scale grid storage applications [1]. Among various cathode materials, manganese dioxide (MnO_2) is notable for its high theoretical capacity of 616 mAh g^{-1}, enabled by a two-electron redox process (Mn^{4+}/Mn^{2+}), as well as the natural abundance, low toxicity, and low cost of manganese [2–4]. Electrolytic manganese dioxide (EMD) is widely employed in commercial Zn-ion batteries due to its well-controlled microstructure and crystallinity, which enable reproducible electrochemical performance and enhanced cycling stability [5]. However, MnO_2 exists in multiple polymorphs, each with distinct crystal structures and electrochemical properties, leading to discrepancies in the reaction mechanisms reported across literature. In aqueous $MnSO_4/H_2SO_4$ electrolytes, electrochemical deposition upon charging consistently yields

ε-MnO_2 regardless of electrolyte concentration, current density, or substrate [6]. Furthermore, studies have shown that, regardless of the initial phase, whether β-MnO_2 or γ-MnO_2, the ε-MnO_2 phase forms during redeposition in subsequent charging cycles in $ZnSO_4$/$MnSO_4$ electrolytes [7]. These observations establish ε-MnO_2 as a recurring and critical phase in acidic aqueous environments, underscoring the need for a fundamental understanding of its behavior to clarify the factors governing reversibility in Zn||MnO_2 batteries.

Tran et al. demonstrated that discharge leads to a partial transformation of EMD into spinel $ZnMn_2O_4$, while simultaneously Zn^{2+} intercalates into the tunnel structures of γ- and ε-MnO_2, producing tunnel-type Zn_xMnO_2 [8]. During the initial cycles, distinct voltage profiles and local pH fluctuations strongly influence the cathode reaction pathway, influencing the overall Zn||MnO_2 electrochemistry [9–11]. The interplay between H^+ and Zn^{2+} insertion and the associated Mn conversion chemistry has been shown to play a central role in governing capacity contributions and electrochemical response [12]. As cycling progresses, the system transitions into a more stable regime where the voltage profiles become reproducible, enabling a clearer investigation of the steady-state reaction mechanism. Understanding this regime is critical, as long-term failure is often driven by electrolyte degradation through parasitic side reactions, namely hydrogen evolution at the Zn anode [13] and byproduct formation and reaction heterogeneities at the MnO_2 cathode, which limit reversibility and cycle life [9, 14, 15].

To address these limitations, several strategies have been explored, including electrolyte additives, such as organic salts, inorganic salts, and water-in-salt, to enhance aqueous Zn-ion batteries, summarized in Table S1. At the Zn anode, these additives have well-established roles, regulating the Zn^{2+} solvation structure, reducing water coordination in the primary solvation shell, suppressing parasitic reactions such as HER and corrosion, and promoting formation of a solid–electrolyte interphase (SEI) layer [16–45]. However, their effects on the cathode are not fully understood; in particular, the impact of additives on proton co-insertion and redox kinetics has not been elucidated. More recently, hybrid aqueous–organic electrolytes and solvent additives have attracted attention for their ability to directly tailor the Zn^{2+} solvation structure and alter electrode–electrolyte interfacial chemistry. Additionally, pH balance, electrolyte solvation regulation, and redox mediation have also been identified as a critical strategy for stabilizing Mn-based cathodes during long-term cycling [46]. For example, Cao et al. demonstrated that addition of dimethyl sulfoxide (DMSO) to a $ZnCl_2$–H_2O electrolyte suppressed water reduction and Zn dendrite formation by replacing H_2O in the Zn^{2+} solvation sheath. This effect arises from the higher Gutmann donor number of DMSO (29.8) compared to water (18), leading to improved Zn^{2+} reversibility in Zn||MnO_2 full cells [47]. Similarly, Kao-ian et al. reported enhanced Zn^{2+} reversibility and reduced formation of spinel-$ZnMn_2O_4$ in δ-MnO_2 cathodes when using ZnTFSi electrolytes with DMSO as the solvent, as confirmed by X-ray diffraction (XRD) analysis of cycled electrodes [48]. Despite these advances, there remains a need to investigate steady-state cycling conditions in Zn||MnO_2 batteries to determine how reducing water activity modifies cathode reaction pathways.

In this work, we investigate the crystalline phase evolution of ε-MnO_2 during the steady regime of cycling after extended conditioning when electrochemical and structural responses become consistent over cycles using operando synchrotron XRD, quantifying lattice changes, phase fractions, and Zn occupancy. These measurements reveal a persistent dual-ion intercalation mechanism (H^+/Zn^{2+}), with an increasing contribution from Zn^{2+}. To further probe electrolyte effects on cathode reaction mechanism, DMSO is introduced as a co-solvent to reduce water activity and reorganize the solvation structure. Under these conditions, electrolyte structure and interfacial chemistry couple to enhance the reversibility of Zn^{2+} intercalation, as confirmed by operando diffraction, despite moderately slower transport. Complementary XPS depth profiling indicates that DMSO mitigates the variation of surface-to-subsurface Mn oxidation-state observed in cells cycled without DMSO. Together, these findings demonstrate that tuning electrolyte solvation can suppress parasitic pathways and stabilize cathode intercalation mechanisms. More broadly, this work shifts electrolyte-additive design from an anode-centric focus (e.g., HER suppression) to a whole-cell perspective, offering strategies to improve the reversibility and durability of mild-aqueous Zn||MnO_2 systems.

2 | Results and Discussion

The ε-MnO_2 cathode was synthesized via constant-current electrodeposition. Briefly, electrodeposition was carried out from an aqueous electrolyte containing 1 M $ZnSO_4$, 0.5 M $MnSO_4$, and 0.1 M H_2SO_4 onto a multi-walled carbon nanotube (MWCNT)-coated carbon cloth substrate, with Zn foil serving as the counter electrode.

To investigate the mechanisms governing steady-state cycling behavior, the Zn||ε-MnO_2 battery was precycled for ~100 hours prior to operando measurements. This preconditioning period allows the system to evolve beyond the initial formation stage, which is associated with irreversible structural changes including partial spinel $ZnMn_2O_4$ formation and active material reorganization as documented in prior literature [7–9]. As shown in Figure S1, the discharge and charge capacities stabilize after this period, indicating the establishment of a steady-state regime with reproducible electrochemical response. Operando XRD confirms that the ε-MnO_2 framework persists after preconditioning, demonstrating that the cathode retains its structural integrity into the steady-state regime. Figure 1a presents the waterfall plot of the operando synchrotron XRD data for two representative cycles following precycling. The dotted lines correspond to the reference peaks of ε-MnO_2 from the PDF standard (04-005-4883) and appear shifted to lower q relative to the reference positions, consistent with lattice expansion of the ε-MnO_2 cathode. This is likely due to residual Zn^{2+}/H^+ intercalation and partial reduction, which can leave the structure slightly expanded and/or transformed toward reduced layered/spinel-like domains, consistent with a mixed intercalation-conversion reaction pathway in aqueous Zn||MnO_2 cells [9, 49, 50]. Throughout these two cycles, the ε-MnO_2 reflections exhibit a uniform and reversible shift in peak position, consistent with a homogeneous intercalation–deintercalation process involving H^+, Zn^{2+}, or both species. The (001) reflection of zinc hydroxide sulfate (ZHS, 04-012-8189) is

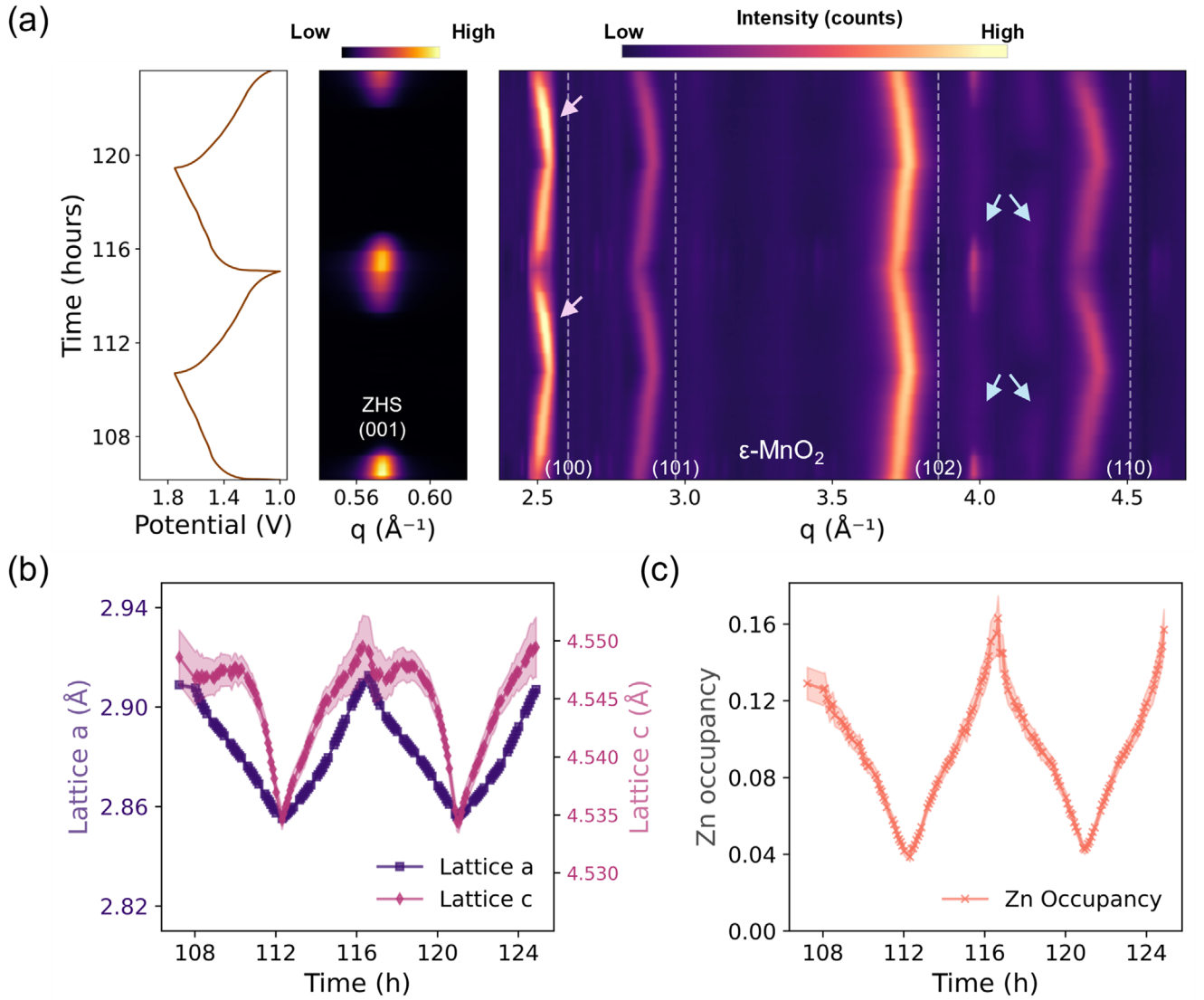

FIGURE 1 | Structural evolution of the ε-MnO_2 electrode in 1 M $ZnSO_4$ electrolyte during stable cycling. (a) Potential profiles and corresponding operando X-ray diffraction waterfall plots showing the evolution of the ZHS (001) reflection and the ε-MnO_2 (100), (101), (102), and (110) reflections (dotted lines showing PDF standard, 04-005-4883). Pink arrows indicate increasing peak intensity, while blue arrows denote the emergence of broader, more disordered peaks. (b) Rietveld refinement results showing the evolution of lattice parameters a and c for ε-MnO_2 during cycling. (c) Zn occupancy (Zn OCC) in the ε-MnO_2 lattice during electrochemical cycling. The curve width reflects the one-sigma fitting uncertainty from the Rietveld analysis.

most prominent at the end of discharge and during the early stages of charge, consistent with reversible local interfacial pH variation during cycling, as also reported in prior studies of ZHS evolution in aqueous Zn||EMD-MnO_2 systems [8]. The reversible appearance and disappearance of ZHS under these stable cycling conditions further suggest that proton-coupled electro-dissolution remains limited. The (001) reflection of zinc hydroxide sulfate (ZHS, 04-012-8189) is most prominent at the end of discharge and during the early stages of charge, suggesting minimal pH fluctuations under these stable cycling conditions, consistent with the minimal proton-coupled electro-dissolution step. These observations indicate that reversible H^+ and/or Zn^{2+} intercalation is the primary contributor to capacity during the steady-state cycling regime of the Zn||MnO_2 battery.

To distinguish between H^+ and Zn^{2+} intercalation in the cathode material, Rietveld refinement was performed to track the evolution of lattice parameters and Zn occupancy. The lattice parameter *a* exhibits a fully reversible change from 2.91 to 2.85 Å during electrochemical cycling, whereas the lattice parameter *c* shows a smaller variation, from 4.550 to 4.535 Å, with the most pronounced change occurring near the end of charge and the beginning of discharge (see Figure 1b). The Zn occupancy in ε-MnO_2 varies between 0.04 and 0.16 (Figure 1c), gradually increasing during discharge and decreasing during charge. The corresponding change in zinc content (Δx ~0.12) enables estimation of the capacity contribution from Zn^{2+} intercalation using Faraday's law. This yields a capacity of ~74 mAh g^{-1} attributable to Zn^{2+} intercalation. Given that the total reversible capacity in this steady-state regime is ~200 mAh g^{-1}, Zn^{2+} intercalation accounts for only ~37.5% of the total capacity, with the remaining capacity arising predominantly from proton insertion. Additionally, the Zn occupancy in ε-MnO_2, refined by allowing partial substitution of Zn at the Mn site

($0 < Zn_{occ} < 0.5$) in the Rietveld model (see Experimental Procedures Section in the Supporting Information), is marginally higher (during charge) after successive cycles, indicating that a fraction of Zn^{2+} remains trapped and the intercalation–deintercalation process is not fully reversible. An additional feature in the operando XRD waterfall plot is an increase in peak intensity near 2.5 $Å^{-1}$ prior to the end of discharge, highlighted by the pink arrow in Figure 1a. Broad secondary peaks, indicated by the blue arrows, are also observed in the waterfall plot and in the overlay XRD plot in Figure S2. These features are attributed to the reversible formation of nanodomain spinel $ZnMn_2O_4$ (PDF 04-002-4954), which may nucleate on the surface of the MnO_2, as described by Equation (1).

$$2H_xMnO_{2(s)} + Zn(OH)_{2(s)} \rightarrow ZnMn_2O_{4(s)} + (x+1)\,H_2O_{(l)} \quad (1)$$

This interpretation is supported by TEM studies on EMD-MnO_2 and α-MnO_2 systems, which report the formation of Hetaerolite ($ZnMn_2O_4$) nanodomains during discharge [4, 8, 51]. While the spinel phase has previously been reported in MnO_2 electrodes as an irreversible transformation associated with capacity fading and failure in Zn||MnO_2 batteries, here it appears to form reversibly under stable cycling conditions [14, 15]. The increased XRD peak intensity near 2.5 $Å^{-1}$ likely arises from the overlap of the ε-MnO_2 (100) reflection and the primary spinel $ZnMn_2O_4$ peak corresponding to (211) plane. Due to the broad nature of these reflections, the spinel phase could not be refined quantitatively.

In summary, the reaction mechanism during steady-state cycling is dominated by the intercalation of both H^+ and Zn^{2+}, accompanied by the reversible formation of a nanodomain spinel phase toward the end of discharge. To investigate how this mechanism is influenced by the presence of an organic co-solvent in the electrolyte, we next examine the effect of DMSO on electrolyte properties, specifically its ability to reduce water activity. Figure 2a schematically illustrates the Zn||ε-MnO_2 cell with a DMSO-containing $ZnSO_4$ electrolyte, highlighting the altered solvation environment and its potential impact on ion insertion.

The short-range order of solution structures of liquid electrolytes was evaluated by WAXS. Figure 2b shows the X-ray scattering results for varying concentrations of $ZnSO_4$. The broad peak centered around ~2.0 and ~ 2.9 $Å^{-1}$ are associated with the oxygen–oxygen and oxygen-hydrogen correlations of the hydrogen bonded network of H_2O molecules (i.e., bulk water). With increasing concentrations of $ZnSO_4$, a broad feature near ~1.4–1.7 $Å^{-1}$ becomes apparent, which is consistent with the presence of contact-ion-pairs (CIP; $Zn^{2+}\cdots SO_4^{2-}$) as previously reported for $ZnSO_4$ electrolytes [52]. On addition of the $ZnSO_4$ salt the bulk-water maximum shifts to higher q relative to water, consistent with a tighter local water structure in the Zn^{2+} hydration environment. The effect of DMSO on the solvation structure is illustrated in Figure 2c,d for 1 M and 2 M $ZnSO_4$ for varying DMSO volume fractions. The bulk water and CIP peak positions in the $ZnSO_4$ electrolytes were then determined by using one or two component Gaussian fits within fixed q windows (CIP: ~1.4–1.7 $Å^{-1}$; bulk water: ~1.8–2.2 $Å^{-1}$). The error bars shown represent the standard errors of the fitted peak positions, as obtained from the fit covariance. Increasing DMSO fraction progressively attenuates and shifts the bulk-water band towards a lower q (Figure 2e). To further verify that the observed changes in the WAXS signal are attributable to electrolyte restructuring, difference curves were computed by subtracting the scattering of the corresponding water + X% DMSO solution from each $ZnSO_4$ + X% DMSO sample for both 1 M and 2 M $ZnSO_4$ (Figure S3). These difference curves confirm a robust and systematic disruption of the bulk water network with increasing DMSO content, while revealing no distinct concentration-dependent feature in the CIP region, consistent across both salt concentrations.

Increasing DMSO fraction progressively attenuates and shifts the bulk-water band toward lower q indicating expansion of the hydrogen-bond network. This effect is most pronounced in pure water and is moderated by dissolved $ZnSO_4$, with the moderation being more evident at 1 M concentration. These results suggest that Zn^{2+} hydration partially offsets the DMSO-driven reorganization of water. The difference scattering analysis (Figure S3) confirms that DMSO's primary effect is on the bulk water network. The conductivity measurements (Figure S4) show an overall decreasing trend with increasing DMSO. Instead, a competing effect dominates: Feng et al. report that DMSO coordinates more strongly to Zn^{2+} than H_2O, forming mixed $[Zn(H_2O)_m(DMSO)_n]^{2+}$ complexes with larger radii than $[Zn(H_2O)_6]^{2+}$, which slows Zn^{2+} diffusion [21]. Along with higher viscosity and reduced water activity, these enlarged solvation shells hinder ion mobility.

Overall, DMSO mainly perturbs the bulk water network, while ion pairing between Zn^{2+} and SO_4^{2-} remains comparatively robust and only weakens at higher $ZnSO_4$ and DMSO concentration (2 M $ZnSO_4$, 25% by volume of DMSO). This difference between solvent reorganization and ion-pair stability helps explain the observed decrease in ionic conductivity with increasing DMSO content. To probe the impact of solvation structure on the reaction mechanism of ε-MnO_2 electrodes, an electrolyte containing 25 vol.% DMSO was selected for detailed operando and electrochemical studies. WAXS analysis (Figure 2c–e) shows that while lower DMSO contents (5%–10%) only weakly perturb the water structure, 25 vol.% induces a pronounced attenuation and shift of the bulk water peak, indicating significant disruption of the hydrogen-bond network and reduced water activity.

This composition represents a balance between modifying the solvation environment and preserving electrochemical functionality, as higher DMSO contents further decrease ionic conductivity and increase viscosity (Figure S3). Accordingly, 25 vol.% DMSO provides a suitable regime to investigate solvation-driven effects on cathode reversibility without excessively compromising cell kinetics. Cells cycled in 1 M $ZnSO_4$ with and without 25 vol.% DMSO (Figure 3). Figure 3a shows the Zn occupancy in ε-MnO_2 obtained by Rietveld refinement, comparing electrolytes with and without 25 vol.% DMSO in 1 M $ZnSO_4$. Representative Rietveld refinement profiles for the charged and discharged states are provided in the Supporting Information for cells cycled without DMSO (Figure S5) and with 25 vol.% DMSO (Figure S6), confirming good agreement between observed and calculated profiles across all conditions. In the additive-free electrolyte, Zn occupancy increases progressively with cycling, indicating limited reversibility and gradual accumulation of irreversibly trapped Zn^{2+} within the cathode structure (see blue dashed lines).

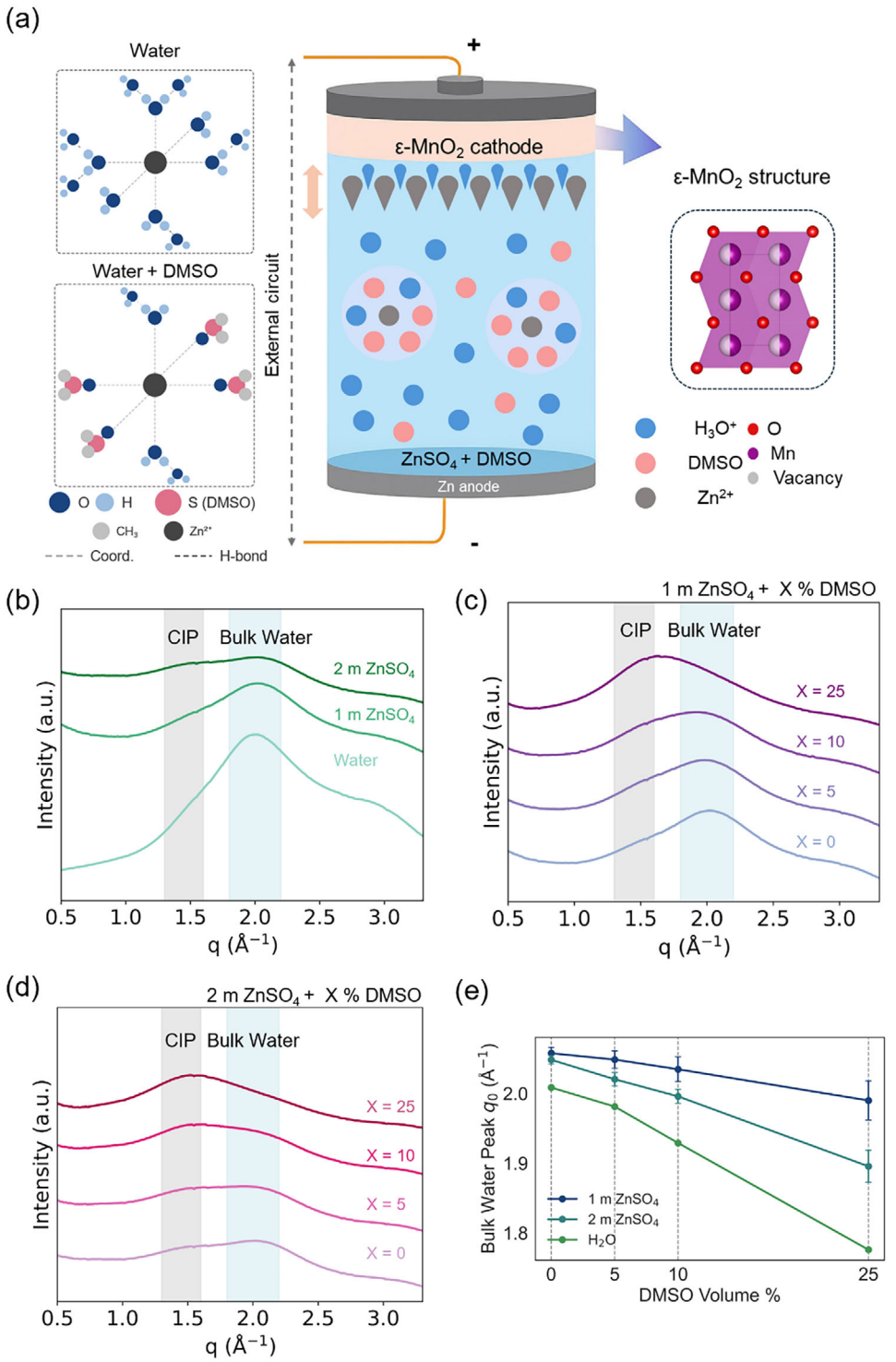

FIGURE 2 | Effect of DMSO on bulk water and contact ion pair (CIP) structure in aqueous $ZnSO_4$ electrolytes. (a) Schematic representation of changes to solvation structure upon DMSO incorporation in aqueous Zn||MnO_2 batteries. H^+ is denoted as H_3O^+ in the schematic to represent proton carriers in aqueous solution. (b) X-ray scattering spectra for water, 1 M $ZnSO_4$, and 2 M $ZnSO_4$, highlighting the CIP (~1.55 $Å^{-1}$) and bulk water (~2.0 $Å^{-1}$) regions. X-ray scattering curves for (c) 1 M $ZnSO_4$ and (d) 2 M $ZnSO_4$ as a function of DMSO volume fraction (X = 0%, 5%, 10%, 25%). Quantified peak positions for (e) bulk water (left) as a function of DMSO volume fraction.

For the DMSO-containing electrolyte, Zn occupancy increases gradually during the first three cycles (Figure S7) but then stabilizes at a consistently lower level compared to the additive-free case (see red dashed line in Figure 3a). This demonstrates that reducing water activity with DMSO suppresses irreversible Zn insertion-extraction despite the lower ionic conductivity of the electrolyte.

The Zn^{2+} capacity contribution was estimated during the discharge half-cycle change in Zn occupancy obtained by Rietveld

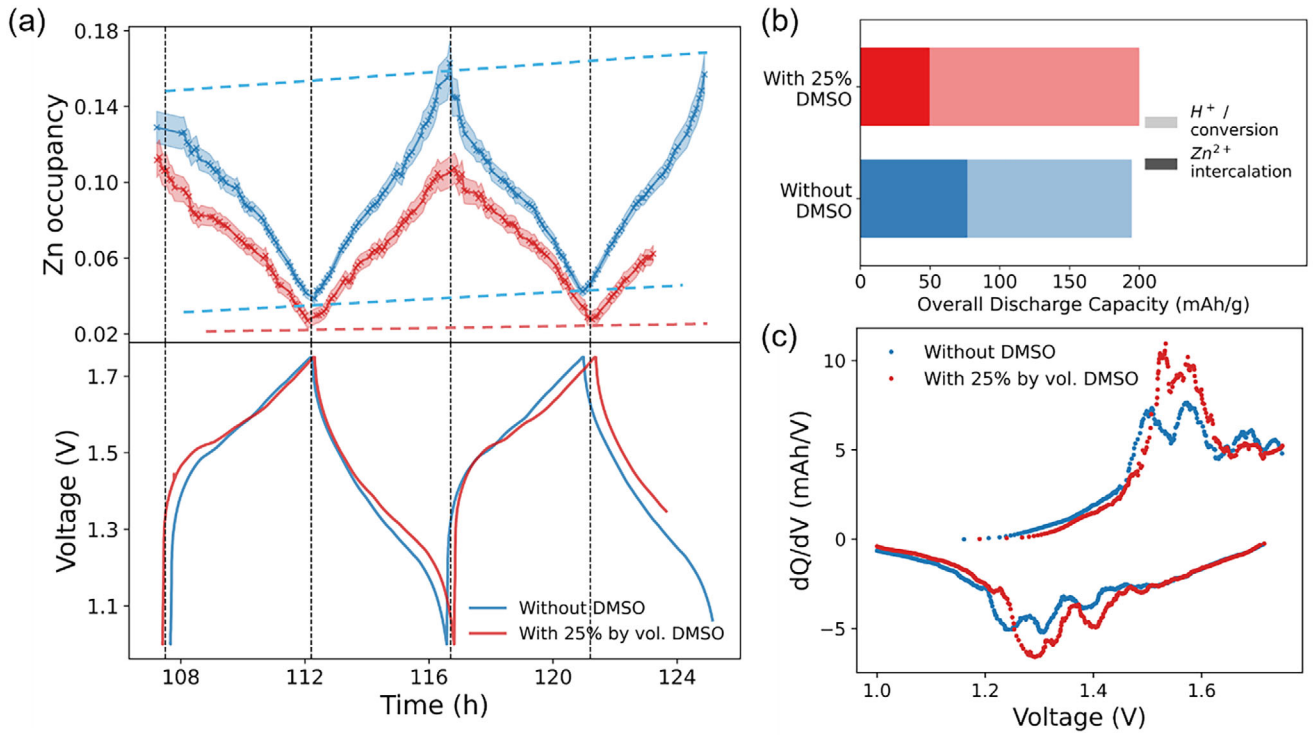

FIGURE 3 | Effect of DMSO additive on the reaction mechanism of ε-MnO_2 cathodes during stable cycling conditions. (a) Zn occupancy of the ε-MnO_2 comparison between without DMSO additive and with 25% by vol. DMSO, quantified by Rietveld refinement. (b) Quantitative breakdown of Zn^{2+} intercalation and remaining capacity contributions (encompassing H^+ intercalation and conversion reactions) to the overall discharge capacity for cells cycled with and without DMSO. (c) The differential capacity vs voltage profile comparison with and without DMSO additive for the cycled ε-MnO_2.

refinement, with the remaining capacity attributed to H^+ intercalation and other conversion reactions including MnO_2 dissolution and spinel $ZnMn_2O_4$ formation (Figure 3b). This analysis reveals that the DMSO-containing electrolyte exhibits a proportionally larger H^+ and conversion reaction contribution relative to Zn^{2+} compared to the additive-free electrolyte, consistent with reduced water activity moderating Zn^{2+} insertion while suppressing irreversible Zn^{2+} accumulation within the lattice.

Figure 3b compares the differential capacity (*dQ/dV*) profiles of cycled ε-MnO_2 electrodes with and without the DMSO additive. During charge, the profile with DMSO additive exhibits a more distinct peak at higher potential, whereas the response without additive is broader and shifted to lower potential. Such differences may reflect changes in reaction selectivity or side processes [7], as reported in prior Zn/MnO_2 studies, competing with reversible Zn and proton deintercalation. Meanwhile, the discharge profiles with DMSO show more pronounced peaks compared to the additive-free electrolyte, indicating improved Zn^{2+} and H^+ reinsertion and overall enhanced reversibility. Together, these results highlight that while DMSO reduces ionic conductivity, its ability to regulate solvation and lower water activity mitigates parasitic reactions and stabilizes Zn insertion–extraction in ε-MnO_2 cathodes.

To further evaluate the improved reversibility of aqueous Zn||MnO_2 batteries with DMSO additives, surface-sensitive XPS studies were carried out, as the electrode surface plays a decisive role in governing subsequent electrochemical reactions. Mn 3s spectra were analyzed for cycled electrodes extracted from Zn||MnO_2 cells with and without DMSO after ~300 h of operation in 1 M $ZnSO_4$ + 0.1 M $MnSO_4$ electrolyte.

Comparison of Mn 3s splitting before and after 600 s of sputtering reveals a distinct shift toward lower binding energy for the electrode cycled without DMSO (Figure 4a), consistent with a more reduced Mn state near the electrode surface. In contrast, the electrode from the DMSO-containing electrolyte shows negligible change after sputtering, suggesting a more stable surface chemistry. Notably, the Mn 3s features in the presence of DMSO exhibit broader profiles compared to the control. This lower apparent resolution is attributed to the diverse coordination environments created by Mn-DMSO interactions at the electrode surface, leading to inhomogeneous broadening, which is further corroborated by the O 1s spectra (Figure S8) showing a larger relative contribution from surface oxygen species in the DMSO-containing electrode compared to the control. Together, these observations suggest that DMSO modifies the local surface chemistry of the electrode. The average oxidation states (Figure 4b): electrode cycled without DMSO exhibits a pronounced increase in average oxidation state upon sputtering (3.31 → 3.48), indicative of a more pronounced surface enriched in reduced Mn^{3+} species, plausibly associated with a spinel-like $ZnMn_2O_4$ surface phase. By contrast, the DMSO electrolyte maintains a higher and more uniform Mn oxidation state (3.44 → 3.42), suggesting improved reversibility and a more homogeneous electrode bulk. Rather than completely preventing spinel-like $ZnMn_2O_4$ formation, the DMSO-containing electrolyte appears to minimize its extent and accumulation, consistent with suppression of irreversible surface phase growth and improved structural reversibility. The

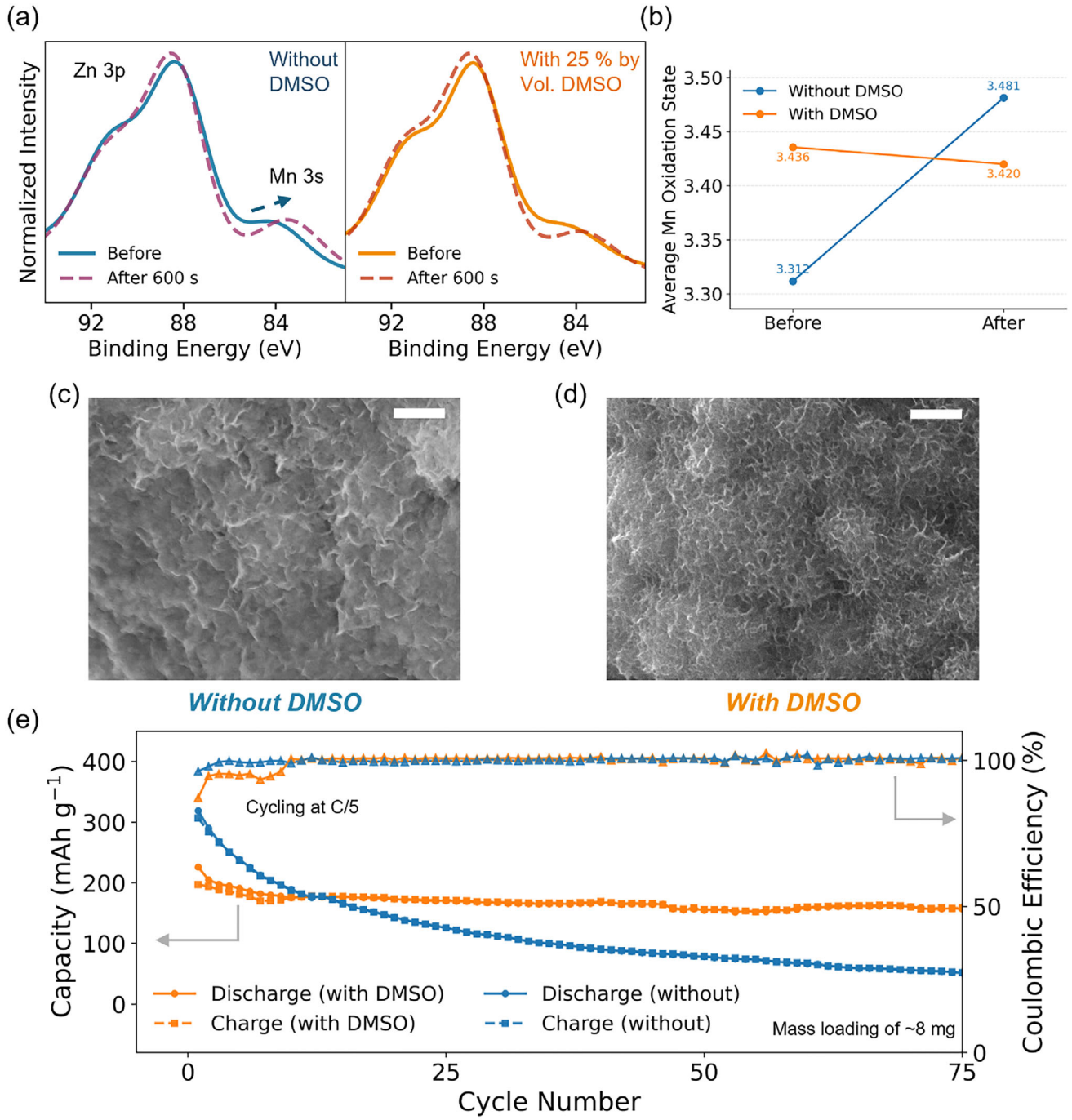

FIGURE 4 | XPS and electrochemical comparison of Zn||MnO_2 cells cycled with and without DMSO additive. (a) Area-normalized Zn 3p, Mn 3s XPS overlays for cycled ε-MnO_2 cathodes without DMSO (left) and with 25 vol. % DMSO (right), plotted before (solid line) and after 600 s argon sputtering (dashed line). The blue arrow indicates the shift of Mn 3s towards lower binding energy. (b) Average Mn oxidation state before/after sputter indicating a thinner reduced surface layer with DMSO. (c,d) SEM images of ε-MnO_2 electrodes cycled without DMSO (c) and with 25 vol.% DMSO (d), scale bars: 1 μm. (c) Galvanostatic cycling discharge/charge capacity and coulombic efficiency vs cycle number for both 1 M $ZnSO_4$ + 0.1 M $MnSO_4$ with and without 25 vol. % DMSO; electrolyte with DMSO shows higher capacity retention over 75 cycles.

average oxidation state was determined by deconvoluting the Mn 2p XPS spectra into Mn^{3+} and Mn^{4+} contributions and subsequently verified through the multiplet splitting of the Mn 3s spectra, as described in the Experimental Procedures section. The Mn 2p and Mn 3s deconvolution, together with the O 1s and Zn 2p spectra of the electrodes, are provided in Figures S8–S11.

After 100 h of cycling, the SEMs of electrodes extracted at the charge states reveal notable morphological differences between the two electrodes (Figure 4c,d). The electrode cycled without DMSO exhibits a rougher, more uneven surface with greater porosity between particles, consistent with heterogeneous dissolution and redeposition processes driven by parasitic reactions at the cathode surface. In contrast, the DMSO-containing

electrode displays a more uniform and finer-textured morphology, consistent with the suppression of these interfacial side reactions. These observations further corroborate the XPS and operando XRD findings, confirming that the improved cycling stability with DMSO arises from stabilization of the electrode-electrolyte interface rather than morphological modification of the bulk electrode structure.

Electrochemical cycling further corroborates these findings (Figure 4c). The DMSO-containing electrolyte exhibits superior long-term stability, with significantly enhanced capacity retention over extended cycles. Although the initial discharge capacity is lower compared to the cell without DMSO, this is likely due to reduced ionic conductivity and slower mass transport arising from DMSO addition. Nonetheless, the stable cycling profile highlights that reducing water activity and stabilizing the Mn redox chemistry by improved reversibility of H^+ and Zn^{2+} ions outweighs the initial kinetic penalty.

While the initial discharge capacity is lower in the DMSO-containing cell, this is attributable to reduced ionic conductivity and slower mass transport arising from DMSO addition. The similar coulombic efficiency observed in both cells reflects proportional fading of both charge and discharge capacities in the cell without DMSO, rather than true reversibility a distinction that is more sensitively captured by the operando XRD, XPS, and SEM results discussed above. Nonetheless, the stable long-term cycling profile of the DMSO-containing cell highlights that the benefits of reduced water activity outweigh the initial kinetic penalty.

Instead, reversibility is governed by interfacial reaction selectivity rather than bulk transport. The formation of $[Zn(H_2O)_m(DMSO)_n]^{2+}$ complexes lowers free water activity, suppressing irreversible Zn^{2+} insertions and phase transformation and promoting reversible proton intercalation. Consequently, the reaction pathway shifts toward a slower but more selective and reversible intercalation process.

3 | Conclusions

In this work, we present a mechanistic understanding of aqueous Zn||ε-MnO_2 batteries cycled under stable cycling conditions. Operando synchrotron X-ray techniques reveal that stable cycling proceeds predominantly through combined H^+ and Zn^{2+} intercalation, accompanied by the formation of short-range nanodomains. The reaction mechanism is further understood upon introduction of co-solvent DMSO into the electrolyte. Wide-angle X-ray scattering of $ZnSO_4$-DMSO electrolytes shows that DMSO primarily perturbs the bulk water network, while ion pairing remains comparatively robust and only weakens at higher salt concentrations. This decoupling between solvent reorganization and ion-pair structure explains the composition-dependent transport and interfacial behavior observed in these mixed electrolytes. Despite slower ion transport kinetics, operando diffraction demonstrates that DMSO significantly enhances the reversibility of Zn^{2+} intercalation. Complementary XPS shows that cells cycled without DMSO develop a pronounced change in Mn oxidation state between the surface and subsurface region, whereas with DMSO the oxidation state remains nearly unchanged throughout the depth profile. Overall, we show that tailoring electrolyte solvation structure can stabilize interfacial chemistry and enhance redox reversibility of the manganese oxide cathodes, even when ion transport is kinetically limited. This work highlights that improving interfacial reaction selectivity, rather than maximizing bulk ion transport, is critical for achieving durable Zn||MnO_2 battery performance. These findings provide valuable design guidelines for advancing durable and efficient aqueous Zn||MnO_2 battery systems.

Acknowledgements

This research was supported by the Center for Mesoscale Transport Properties, an Energy Frontier Research Center supported by the U.S. Department of Energy, Office of Science, Basic Energy Sciences, under award #DE-SC0012673. This research used resources, X-ray Powder Diffraction beamline (XPD, 28-ID-2) and Complex Materials Scattering beamline (CMS, 11-BM) of the National Synchrotron Light Source II, a U.S. Department of Energy (DOE) Office of Science by Brookhaven National Laboratory under Contract No. DE-SC0012704. This research used the Materials Synthesis and Characterization Facility of the Center for Functional Nanomaterials (CFN), which is a U.S. Department of Energy Office of Science User Facility, at Brookhaven National Laboratory under Contract No. DE-SC0012704. We thank the support of Data Science and System Integration staff, Steven LaMarra, and XPD beamline staff, John Trunk, for support in setting up operando experiment. EST acknowledges the support of the William and Jane Knapp Chair in Energy and the Environment.

Conflicts of Interest

The authors declare no conflicts of interest.

Data Availability Statement

The data that support the findings of this study are available on request from the corresponding author. The data are not publicly available due to privacy or ethical restrictions.

References

1. S. Liu, R. Zhang, C. Wang, et al., "Zinc ion Batteries: Bridging the Gap from Academia to Industry for Grid-Scale Energy Storage," *Angewandte Chemie International Edition* 63, no. 17 (2024): 202400045, https://doi.org/10.1002/anie.202400045.

2. H. Moon, K. H. Ha, Y. Park, et al., "Direct Proof of the Reversible Dissolution/Deposition of Mn^{2+}/Mn^{4+} for Mild-Acid Zn-MnO_2 Batteries with Porous Carbon Interlayers," *Advancement of Science* 8, no. 6 (2021): 2003714, ttps://doi.org/10.1002/advs.202003714.

3. D. Wu, L. M. Housel, S. J. Kim, et al., "Quantitative Temporally and Spatially Resolved X-Ray Fluorescence Microprobe Characterization of the Manganese Dissolution-Deposition Mechanism in Aqueous Zn/α-MnO_2 Batteries," *Energy and Environmental Science* 13, no. 11 (2020): 4322–4333, https://doi.org/10.1039/D0EE02168G.

4. S. J. Kim, D. Wu, N. Sadique, et al., "Unraveling the Dissolution-Mediated Reaction Mechanism of α-MnO_2 Cathodes for Aqueous Zn-Ion Batteries," *Small* 16, no. 48 (2020): 2005406, https://doi.org/10.1002/smll.202005406.

5. A. Biswal, B. Chandra Tripathy, K. Sanjay, T. Subbaiah, and M. Minakshi, "Electrolytic Manganese Dioxide (Emd): A Perspective on Worldwide Production, Reserves and Its Role in Electrochemistry," *RSC Advances* 5, no. 72 (2015): 58255–58283, https://doi.org/10.1039/C5RA05892A.

6. X. Xiao, Z. Zhang, Y. Wu, et al., "Ultrahigh-Loading Manganese-Based Electrodes for Aqueous Batteries via Polymorph Tuning," *Advanced*

Materials 35, no. 33 (2023): 2211555, https://doi.org/10.1002/adma.202211555.

7. I. Aguilar, P. Lemaire, N. Ayouni, et al., "Identifying Interfacial Mechanisms Limitations within Aqueous Zn-MnO_2 Batteries and Means to Cure them with Additives," *Energy Storage Materials* 53 (2022): 238–253, https://doi.org/10.1016/j.ensm.2022.08.043.

8. T. N. T. Tran, S. Jin, M. Cuisinier, B. D. Adams, and D. G. Ivey, "Reaction Mechanisms for Electrolytic Manganese Dioxide in Rechargeable Aqueous Zinc-Ion Batteries," *Scientific Reports* 11, no. 1 (2021): 20777, https://doi.org/10.1038/s41598-021-00148-2.

9. V. R. Kankanallu, X. Zheng, D. Leschev, et al., "Elucidating a Dissolution–Deposition Reaction Mechanism by Multimodal Synchrotron X-ray Characterization in Aqueous Zn/MnO_2 Batteries," *Energy and Environmental Science* 16, no. 6 (2023): 2464–2482, https://doi.org/10.1039/D2EE03731A.

10. L. Godeffroy, I. Aguilar, J. Médard, D. Larcher, J.-M. Tarascon, and F. Kanoufi, "Decoupling the Dynamics of Zinc Hydroxide Sulfate Precipitation/Dissolution in Aqueous Zn–MnO_2 Batteries by Operando Optical Microscopy: A Missing Piece of The Mechanistic Puzzle," *Advanced Energy Materials* 12, no. 30 (2022): 2200722, https://doi.org/10.1002/aenm.202200722.

11. O. Fitz, C. Bischoff, M. Bauer, et al., "Electrolyte Study with in Operando pH Tracking Providing Insight into the Reaction Mechanism of Aqueous Acidic Zn//MnO_2 Batteries," *ChemElectroChem* 8, no. 18 (2021): 3553–3566, https://doi.org/10.1002/celc.202100888.

12. H. Yang, T. Zhang, D. Chen, et al., "Protocol in Evaluating Capacity of Zn–Mn Aqueous Batteries: A Clue Of Ph," *Advanced Materials* 35, no. 24 (2023): 2300053, https://doi.org/10.1002/adma.202300053.

13. J. Chen, W. Zhao, J. Jiang, et al., "Challenges and Perspectives of Hydrogen Evolution-Free Aqueous Zn-Ion Batteries," *Energy Storage Materials* 59 (2023): 102767, https://doi.org/10.1016/j.ensm.2023.04.006.

14. S. Cui, D. Zhang, and Y. Gan, "The effect of Mn2+ additives on the Capacity of Aqueous Zn/δ-MnO_2 Batteries: Elucidating the Mn^{2+} Concentration Dependence of the Irreversible Transformation of δ-MnO_2," *Journal of Power Sources* 579 (2023): 233293, https://doi.org/10.1016/j.jpowsour.2023.233293.

15. L. Li, T. K. A. Hoang, J. Zhi, M. Han, S. Li, and P. Chen, "Functioning Mechanism of the Secondary Aqueous Zn-β-MnO_2 Battery," *ACS Applied Materials Interfaces* 12, no. 11 (2020): 12834–12846, https://doi.org/10.1021/acsami.9b22758.

16. V. J. Ariyamparambil, N. Kim, S. Y. Lee, X. Crispin, T. Park, and Z. Khan, "Water-in-Salt Hydrogel Electrolyte for Dendrite-Free Zn Deposition," *Energy Advances* 4, no. 9 (2025): 1167–1178, https://doi.org/10.1039/d5ya00169b.

17. J. Cao, Y. Jin, H. Wu, et al., "Enhancing Zinc Anode Stability with Gallium Ion-Induced Electrostatic Shielding and Oriented Plating," *Advanced Materials* 15, no. 6 (2025): 2403175, https://doi.org/10.1002/aenm.202403175.

18. J. Cao, D. Zhang, Y. Yue, et al., "Regulating Solvation Structure to Stabilize Zinc Anode by Fastening the Free Water Molecules With an Inorganic Colloidal Electrolyte," *Nano Energy* 93 (2022): 106839, https://doi.org/10.1016/j.nanoen.2021.106839.

19. J. Cui, X. Liu, Y. Xie, et al., "Improved Electrochemical Reversibility of Zn Plating/Stripping: A Promising Approach to Suppress Water-Induced Issues Through the Formation of H-Bonding," *Materials Today Energy* 18 (2020): 100563, https://doi.org/10.1016/j.mtener.2020.100563.

20. A. Ejigu, L. W. Le Fevre, and R. A. W. Dryfe, "Reversible Electrochemical Energy Storage Based on Zinc-Halide Chemistry," *ACS Applied Mater Interfaces* 13, no. 12 (2021): 14112–14121, https://doi.org/10.1021/acsami.0c20622.

21. D. Feng, F. Cao, L. Hou, T. Li, Y. Jiao, and P. Wu, "Immunizing Aqueous Zn Batteries against Dendrite Formation and Side Reactions at Various Temperatures via Electrolyte Additives," *Small* 17, no. 42 (2021): 2103195, https://doi.org/10.1002/smll.202103195.

22. X. Guo, Z. Zhang, J. Li, et al., "Carbonaceous Sulfur Host for Cathodes in Room-Temperature Metal–Sulfur Batteries," *ACS Energy Letters* 6, no. 2 (2021): 395–403, https://doi.org/10.1021/acsenergylett.0c02371.

23. D. Han, Z. Wang, H. Lu, et al., "A Self-Regulated Interface toward Highly Reversible Aqueous Zinc Batteries," *Advanced Energy Materials* 12, no. 9 (2022): 2102982, https://doi.org/10.1002/aenm.202102982.

24. J. Han, A. Mariani, A. Varzi, and S. Passerini, "Green and Low-Cost Acetate-Based Electrolytes for the Highly Reversible Zinc Anode," *Journal of Power Sources* 485 (2021): 229329, https://doi.org/10.1016/j.jpowsour.2020.229329.

25. P. Hu, M. Yan, T. Zhu, et al., "Zn/V_2O_5 Aqueous Hybrid-Ion Battery with High Voltage Platform and Long Cycle Life," *ACS Applied Materials Interfaces* 9, no. 49 (2017): 42717–42722, https://doi.org/10.1021/acsami.7b13110.

26. H. J. Kim, S. Kim, J. H. Yu, J.-H. Lim, H. Yashiro, and S.-T. Myung, "Unlocking Long-Term Stability: Electrolyte Additives for Suppressing Zinc Dendrite Growth in Aqueous Zinc Metal Batteries," *Chemical Engineering Journal* 506 (2025): 160017, https://doi.org/10.1016/j.cej.2025.160017.

27. Y. Li, P. Wu, W. Zhong, et al., "A Progressive Nucleation Mechanism Enables Stable Zinc Stripping–Plating Behavior," *Energy and Environmental Science* 14, no. 10 (2021): 5563–5571.

28. W. Liang, D. Li, R. Zhong, et al., "Electrolyte Engineering Strategy With Catecholate Type Additive Enabled Ultradurable Zn Anode," *Advanced Functional Materials* 35 (2025): 2504195, https://doi.org/10.1002/adfm.202504195.

29. J. Liu, Z. Shen, and C.-Z. Lu, "Disodium Malate Electrolyte Additive Facilitates Dendrite-Free Zinc Anode: Deposition Kinetics and Interface Regulation," *Small Methods* 9, no. 1 (2025): 2400719, https://doi.org/10.1002/smtd.202400719.

30. K. Liu, M. Sun, Y. Wu, et al., "Binary Electrolyte Additive-Reinforced Interfacial Molecule Adsorption Layer for Ultra-Stable Zinc Metal Anodes," *Advanced Materials* 37, no. 18 (2025): 2420079, https://doi.org/10.1002/adma.202420079.

31. M. Liu, Y. Wang, Y. Li, et al., "Dual-Functional Interfacial Layer Enabled by Gating-Shielding Effects for Ultra-Stable Zn Anode," *Advanced Materials* 36, no. 44 (2024): 2406145, https://doi.org/10.1002/adma.202406145.

32. H. Lu, X. Zhang, M. Luo, et al., "Amino Acid-Induced Interface Charge Engineering Enables Highly Reversible Zn Anode," *Advanced Functional Materials* 31, no. 45 (2021): 2103514, https://doi.org/10.1002/adfm.202103514.

33. M. Luo, T. C. Li, P. Wang, et al., "Dynamic Regulation of the Interfacial pH for Highly Reversible Aqueous Zinc Ion Batteries," *Nano Letters* 23, no. 20 (2023): 9491–9499, https://doi.org/10.1021/acs.nanolett.3c02904.

34. W. Lv, J. Meng, X. Li, et al., "Boosting Zinc Storage in Potassium-Birnessite via Organic-Inorganic Electrolyte Strategy with Slight *N*-methyl-2-Pyrrolidone Additive," *Energy Storage Materials* 54 (2023): 784–793, https://doi.org/10.1016/j.ensm.2022.11.011.

35. Q. Ni, H. Jiang, S. Sandstrom, et al., "A Na3V2 (PO4) 2O1. 6F1. 4 Cathode of Zn-ion Battery Enabled by a Water-in-Bisalt Electrolyte," *Advanced Functional Materials* 30, no. 36 (2020): 2003511, https://doi.org/10.1002/adfm.202003511.

36. Y. Quan, M. Yang, M. Chen, et al., "Electrolyte Additive of Sorbitol Rendering Aqueous Zinc-Ion Batteries with Dendrite-Free Behavior and Good Anti-Freezing Ability," *Chemical Engineering Journal* 458 (2023): 141392, https://doi.org/10.1016/j.cej.2023.141392.

37. P. Sun, L. Ma, W. Zhou, et al., "Simultaneous Regulation on Solvation Shell and Electrode Interface for Dendrite-Free Zn Ion Batteries Achieved by a Low-Cost Glucose Additive," *Angewandte Chemie International Edition* 60, no. 33 (2021): 18247–18255, https://doi.org/10.1002/anie.202105756.

38. S. Tang, Q. Wei, B. Liu, et al., "Simultaneous Manipulation of Electric Double Layer and Zn (100) Deposition Enabled by Anions for Highly Stable Zn Anodes," *Angewandte Chemie International Edition* 64 (2025): 202510252, https://doi.org/10.1002/anie.202510252.

39. D. Wang, D. Lv, H. Liu, et al., "In Situ Formation of Nitrogen-Rich Solid Electrolyte Interphase and Simultaneous Regulating Solvation Structures for Advanced Zn Metal Batteries," *Angewandte Chemie International Edition* 61, no. 52 (2022): 202212839, https://doi.org/10.1002/anie.202212839.

40. F. Wang, O. Borodin, T. Gao, et al., "Highly Reversible Zinc Metal Anode for Aqueous Batteries," *Nature Materials* 17, no. 6 (2018): 543–549, https://doi.org/10.1038/s41563-018-0063-z.

41. T. Xue, Y. Mu, Z. Zhang, et al., "Enhanced Zinc Deposition and Dendrite Suppression in Aqueous Zinc-Ion Batteries Via Citric Acid-Aspartame Electrolyte Additives," *Advanced Energy Materials* 15, no. 26 (2025): 2500674, https://doi.org/10.1002/aenm.202500674.

42. H. Yu, D. Chen, X. Ni, et al., "Reversible Adsorption with Oriented Arrangement of a Zwitterionic Additive Stabilizes Electrodes for Ultralong-Life Zn-Ion Batteries," *Energy and Environmental Science* 16, no. 6 (2023): 2684–2695, https://doi.org/10.1039/D3EE00982C.

43. C. Zhang, J. Holoubek, X. Wu, et al., "A $ZnCl_2$ Water-in-Salt Electrolyte for a Reversible Zn Metal Anode," *Chemical Communications* 54, no. 100 (2018): 14097–14099, https://doi.org/10.1039/C8CC07730D.

44. L. Zhang, I. A. Rodríguez-Pérez, H. Jiang, et al., "$ZnCl_2$ "Water-in-Salt" Electrolyte Transforms the Performance of Vanadium Oxide as a Zn Battery Cathode," *Advaanced Functional Materials* 29, no. 30 (2019): 1902653, https://doi.org/10.1002/adfm.201902653.

45. Z. Zhang, S. Yan, H. Dong, et al., "Investigating the role of Non-Ionic Surfactants as Electrolyte Additives for Improved Zinc Anode Performance in Aqueous Batteries," *Journal of Colloid and Interface Science* 677 (2025): 885–894, https://doi.org/10.1016/j.jcis.2024.08.022.

46. W. Zhou, H. J. Fan, D. Zhao, and D. Chao, "Cathodic Electrolyte Engineering Toward Durable Zn–Mn Aqueous Batteries,"*National Science Review* 10, no. 12 (2023): nwad265, https://doi.org/10.1093/nsr/nwad265.

47. L. Cao, D. Li, E. Hu, et al., "Solvation Structure Design for Aqueous Zn Metal Batteries," *Journal of the American Chemical Society* 142, no. 51 (2020): 21404–21409, https://doi.org/10.1021/jacs.0c09794.

48. W. Kao-ian, M. T. Nguyen, T. Yonezawa, et al., "Highly Stable Rechargeable Zinc-Ion Battery Using Dimethyl Sulfoxide Electrolyte," *Materials Today Energy* 21 (2021): 100738, https://doi.org/10.1016/j.mtener.2021.100738.

49. X. Guo, J. Zhou, C. Bai, X. Li, G. Fang, and S. Liang, "Zn/MnO_2 Battery Chemistry with Dissolution-Deposition Mechanism," *Materials Today Energy* 16 (2020): 100396, https://doi.org/10.1016/j.mtener.2020.100396.

50. Y. Zhang, X. Cui, Y. Liu, et al., "Aqueous Zn-MnO_2 battery: Approaching the Energy Storage Limit with Deep Zn^{2+} Pre-Intercalation and Revealing the Ions Insertion/Extraction Mechanisms," *Journal of Energy Chemistry* 67 (2022): 225–232, https://doi.org/10.1016/j.jechem.2021.09.038.

51. O. Rubel, T. N. T. Tran, S. Gourley, et al., "Electrochemical Stability of $ZnMn_2O_4$: Understanding Zn-Ion Rechargeable Battery Capacity and Degradation," *Journal of Physical Chemistry C* 126 (2022): 10957–10967, https://doi.org/10.1021/acs.jpcc.2c01900.

52. J.-H. Huang, X.-F. Luo, T.-Y. Kuo, et al., "Dual-Salt Aqueous Electrolyte for Enhancing Charge-Storage Properties Of VO_2 Polymorphic Cathodes For Zn-Ion Batteries," *Chemical Engineering Journal* 497 (2024): 154609, https://doi.org/10.1016/j.cej.2024.154609.

Supporting Information

Additional supporting information can be found online in the Supporting Information section.

Supporting File: smll74927-sup-0001-SuppMat.pdf.